NONLINEAR DYNAMICS AND STOCHASTICITY OF CORE GENETIC REGULATION

by

HONGGUANG XI

Presented to the Faculty of the Graduate School of
The University of Texas at Arlington in Partial Fulfillment
of the Requirements
for the Degree of

MASTER OF SCIENCE IN MATHEMATICS

THE UNIVERSITY OF TEXAS AT ARLINGTON

May 2012

To my parents, Dilong Xi and Lingying Yao, for their love and dedication; my supervising professor, Marc Turcotte, for his help and guidance; my wife, Jing Zhou, for her company and support; and my daughter, Yufei, for her brightening my world.

ACKNOWLEDGEMENTS

First and foremost, I am grateful to my supervising professor, Dr. Marc Turcotte, for the help, support, and guidance I received from him throughout the course of my study at UT Arlington.

I thank Dr. JianZhong Su, Dr. Andrzej Korzeniowski, and Dr. Hristo Kojouharov, for helpful comments and discussions, and for taking time to serve in my thesis committee.

I also thank several of my friends: Dr. Lixia Duan, Dr. Zhuoqin Yang, Amrita Pal, and Mengfan Tang, who have helped me throughout my career.

Finally, I would like to express my deep gratitude to my parents and brother for their everlasting support and encouragement. I owe too much to my wife. Without her love and care, I would never get here. Also, thank God for giving us an angel, Yufei, who brings us endless happiness.

April 15, 2012

ABSTRACT

NONLINEAR DYNAMICS AND STOCHASTICITY OF
CORE GENETIC REGULATION

HONGGUANG XI, M.S.

The University of Texas at Arlington, 2012

Supervising Professor: Marc Turcotte

Bacillus subtilis is one of the very well-studied organisms in biology. Recent results show that an alternative competence regulation circuit for this bacterium, differing only in the order of the composite negative feedback loop onto the master competence regulator gene comK, despite presenting equivalent functionality, exhibits physiologically important differences.

It is not clear why Nature only selects a specific gene regulation circuit other than a plethora of equivalent others. Here, we hope, from the point of view of reverse engineering, to discover the fundamental reasons for natural selection of a particular circuit structure over another. Based on the wild-type *Bacillus subtilis* circuit, we add a positive autoregulation feedback loop to the intermediate gene comS in the composite negative feedback loop onto ComK. Since positive feedback loops are most frequently observed in biology, this hypothetical modification of the original circuit is evolutionarily plausible.

We use bifurcation theory to study the dynamical features of the hypothetical gene circuit vs. the feedback strength of the added positive autoregulation loop, and we rely on stochastic simulations to perform *in silico* experiments. We discover the existence of a bistable system: a stable limit cycle and a stable fixed point separated by an unstable limit cycle with a varying height of underlying stochastic potential. This structure is absent from the wild type. The coexistence of the unstable limit cycle and stochastic noise endows the circuit with an ability to trap, shield or switch between its two stable attractors. We study the implications for competence. By calculating the probability of entering competence, we conclude that the hypothetical circuit possesses less ability, compared to the wild-type circuit, to survive the severe environmental stresses. This provides some insight into the natural selection of a particular circuit structure by Evolution.

TABLE OF CONTENTS

LIST OF ILLUSTRATIONS

LIST OF TABLES

CHAPTER 1

INTRODUCTION

1.1 Background

Isogenic cell populations can generate different phenotypes due to epigenetic mechanisms [1]. This heterogeneity is meaningful in enhancing the cellular adaptability to the environmental changes at the population level [2, 3, 4, 5]. In the point view of dynamical systems these different phenotypes can be viewed as bistability or multi-stability [6].

It has been shown mathematically that positive nonlinear feedback regulation is necessary for the experimental observation of bistability and for excitability [7].

Two famous examples of epigenetic phenotypic variation are the lactose utilization [8, 9, 10] and lysis/lysogeny switches [11, 12] in *Escherichia coli*. In these examples theoretical modeling and simulations demonstrate the possible contribution of biochemical noise.

We are concerned with the competence phenotype in the bacterium *Bacillus subtilis*. Competence for transformation is a transient natural ability for *B. subtilis* to perform horizontal gene transfer. It is a regulated cellular state induced by environmental stresses whereby bacteria actively accept exogenous free DNA from the environment, and incorporate it into its own genome [13].

Isogenic populations of *B. subtilis* exhibit two (competent and vegetative) states and therefore can be viewed as a bi-stable system. Between $10 \sim 25\%$ of a wild-type *B. subtilis* culture exhibits competence [13], but this depends on conditions.

In *B. subtilis*, the master regulator of the competence machinery is the transcription factor ComK [14], which binds DNA as a tetramer [15], and activates well over 100 genes [16]. ComK is activated via quorum sensing and it is multiply regulated at the transcriptional level. ComK is also a transcription factor for its own gene (comK), thereby defining a positive feedback loop at the core of the competence network. ComK is degraded proteolytically: the constitutively abundant protein MecA binds ComK and targets the complex for degradation by the ClpP-ClpC proteases. The small protein ComS, induced by the quorum sensing machinery and indirectly inhibited by ComK, releases ComK from the complex, through competitive binding to MecA. This defines a negative feedback loop taking the system out of competence. [17, 18, 19, 20].

Transcriptional, rather than translational noise, is the main source of noise in gene regulatory systems [12]. Intrinsic stochastic fluctuations (noise) in transcription of the comK gene consistent with observed low mRNA transcript numbers induce randomness in the timing of competence excursions [21].

Süel *et al.* [22, 23] showed how entry into competence is a stochastic event that depends on intrinsic noise and that competence excursions (entry followed later in time by concomitant exit) are a consequence of excitability. They abstracted complex regulatory dynamics to a core of necessary and sufficient processes: positive autoregulatory feedback of ComK onto comK, and indirect negative feedback by ComS on the degradation of ComK (see Fig. 1.1(A)). And with the MeKS model [22] of the excitable system they interpreted the experimentally observed competence events.

In the MeKS model, *B. subtilis* resides mostly in the vegetative state at high ComS and low ComK. Occasionally, random biochemical fluctuations make the system cross the separatrix, causing it to undergo a committed long-distance excursion.

The MeKS model provides a consistent prediction of the probability of competence initiation, duration and variation, etc..

It is shown experimentally and theoretically that subtly different competence circuit topologies result in biologically important different noise characteristics [24]. Specifically, model predictions for a mutant *Bacillus subtilis* for which only the order of the negative regulation loop through the intermediary ComS gene was inverted, were confirmed experimentally. The mutant shows a decreased level of noise and behaves more like a regular clock, than an excitable system. It is less efficient at sampling a randomly changing environment making it less desirable than WT, from an evolutionary standpoint.

Herein, we are concerned with the reasons why Evolution might have selected a specific circuit and rejected all other choices based on dynamical features of the genetic network and the functions of biochemical noise. We introduced a minimal modification to the MeKS model by adding positive auto-regulation onto the intermediary gene comS, which we denote comS* (or its product ComS*) (see Fig. 1.1(B)). This paper is about the mathematical consequences induced by regulatory choices both from the deterministic (high molecular numbers) and the more realistic stochastic (low molecular numbers) points of view. We are interested by dynamical features arising from nonlinear dynamics of gene regulatory circuits coupled with intrinsic biochemical noise, and attempt to shed light on "why" random evolutionary choices could have been made.

1.2 Organization

We first described the molecular mechanisms with biochemical reactions (see Section 2.1), stochastic model (see Section 2.2) and deterministic models (see Section 2.3 and Section 2.4). Then, we compared the dynamical features of 6-ODE and

2-ODE systems using phase portrait and bifurcation analysis (see Section 2.5). In Section 2.6 we explained how to calculate nullclines and fixed points. In Section 2.7 we introduced the strategy for parameterization using simulated annealing algorithm. We explained in detail the calculation of time in competence in Section 2.8.

Then, we studied the dynamical features and stochastic behaviors of CircuitOne, traversing the parameter space of bs^* (see Section 3.1.1 - Section 3.1.3). We calculated the probability of entering competence (see Section 3.1.4) and explained the stochastic trap effect endowed by the unstable limit cycle (see Section 3.1.5).

Next, we discussed the importance of the added positive feedback loop and explained the stochastic trap/shield effects by considering the interplays between limit cycles (see Section 3.2).

Finally, we summarized our current work and mentioned the future directions (see Chapter 4).

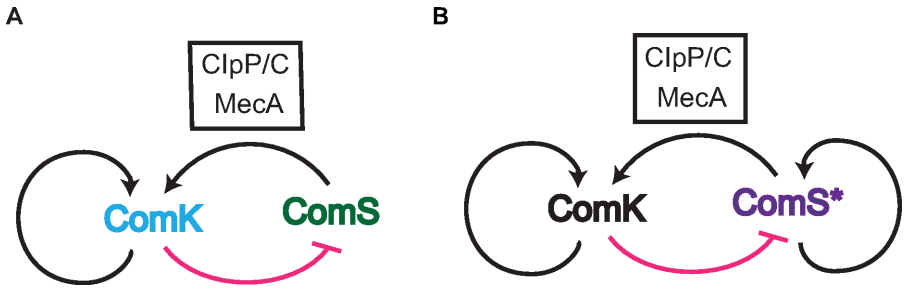

Figure 1.1. **Diagrams of MeKS model and CircuitOne model in *Bacillus subtilis*.** **(A)** Diagram of MeKS model, which is the WT circuit of competence in *B. subtilis*. **(B)** Diagram of CircuitOne model, which is the hypothetical evolutionary plausible circuit similar to WT but has, in addition, a positive auto-regulation of the intermediate gene (comS*).

CHAPTER 2

METHODS

2.1 Biochemical Reactions

We hypothetically present a genetic circuit, called "CircuitOne" (see Figure 1.1(B)), which adds an autoregulation loop to the wild type [22, 23].

The biochemical reactions [22, 23] involved in CircuitOne are

$$
\begin{aligned}
P_{comK}^{const} &\xrightarrow{k_1} P_{comK}^{const} + mRNA_{comK}, \\
P_{comK} &\xrightarrow{f(K,k_2,k_k,n)} P_{comK} + mRNA_{comK}, \\
mRNA_{comK} &\xrightarrow{k_3} mRNA_{comK} + ComK, \\
P_{comS^*}^{const} &\xrightarrow{k_4} P_{comS^*}^{const} + mRNA_{comS^*}, \\
P_{comS^*} &\xrightarrow{g(K,k_5,k_s,p,S^*,b_{ss},s_s,n^*)} P_{comS^*} + mRNA_{comS^*}, \\
mRNA_{comS^*} &\xrightarrow{k_6} mRNA_{comS^*} + ComS^*, \\
mRNA_{comK} &\xrightarrow{k_7} \varnothing, \\
ComK &\xrightarrow{k_8} \varnothing, \\
mRNA_{comS^*} &\xrightarrow{k_9} \varnothing, \\
ComS^* &\xrightarrow{k_{10}} \varnothing, \\
MecA + ComK &\xrightarrow{k_{11}/\Omega} MecA_K, \\
MecA + ComK &\xleftarrow{k_{-11}} MecA_K, \\
MecA_K &\xrightarrow{k_{12}} MecA, \\
MecA + ComS^* &\xrightarrow{k_{13}/\Omega} MecA_S,
\end{aligned}
$$

$$MecA + ComS^* \xleftarrow{k_{-13}} MecA_S,$$
$$MecA_S \xrightarrow{k_{14}} MecA,$$

where P_{comK}^{const} is the constitutive ComK promoter, P_{comK} is the regulated ComK promoter, $mRNA_{comK}$ is the messenger RNA of ComK, $ComK$ is the activator protein, $ComS^*$ is the repressor protein, $MecA$ is another protein to which $ComK$ and $ComS^*$ bind competitively, $MecA_K$ is the dimer of $MecA$ and $ComK$, $k_i, i = 1, ..., 14, -11, -13$, are reaction rates, and all other notations are similar.

Note that k_{11}/Ω and k_{13}/Ω are used in the case when we consider the molecule number of each species. If we consider the concentration of each species, we just use k_{11} and k_{13}.

MecA can negatively control ComK, i.e., when bound by MecA, the gene expression of ComK is inhibited. If by competition more ComS* bind MecA, then more ComK get released, so we can say ComS* (indirectly) enhances the gene expression of ComK.

In the above reactions we describe the activating effect of ComS* on ComK and the positive autoregulation of ComK itself by

$$f(K, k_2, k_k, n) = \frac{k_2 K^n}{k_k^n + K^n}, \tag{2.1}$$

where K is the concentration of ComK (ComS*), k_2 is the strength coefficient, k_k is the concentration of ComK when half comK genes are activated, and n is the Hill coefficient. In total, f behaves as a rate constant.

And, the suppressing effect of ComK on ComS* and the positive autoregulation of ComS* itself are manifested in

$$g(K, k_5, k_s, p, S^*, b_{ss}, s_s, n^*) = \frac{k_5 k_s^p}{k_s^p + K^p} \cdot \frac{b_{ss} S^{*n^*}}{s_s^{n^*} + S^{*n^*}} \tag{2.2}$$

where K (S^*) is the concentration of ComK (ComS*), k_5 is the strength coefficient, k_s is the concentration of ComK when half comS* genes are activated, p and n^* are the Hill coefficients, s_s is the concentration of ComS* when half comS* genes are activated, and b_{ss} is a scaling factor without unit. In total, g behaves as a rate constant.

2.2 Stochastic Model

The stochastic model consists of 16 elemental biochemical reactions (see Section 2.1) that constitute a discrete event level description of mRNA and protein dynamics of the two constituent proteins in the system: ComK and ComS*. Included in this description is mRNA constitutive and regulated production, constitutive degradation, mRNA translation into ComK and ComS*, and their competitive proteolytic degradation via complexing (binding) with free MecA, in the form of ComK_MecA ($MecA_K$) and ComS*_MecA ($MecA_S$). Biochemical fluctuations are simulated using the Gillespie algorithm which numerically reproduces the solution of the equivalent Master Equation of the system [25, 26, 27, 28].

2.3 The 6-ODE Deterministic Model

2.3.1 Model Description

Based on all those reactions (see Section 2.1) we can write six reaction rate functions:

$$\frac{d[mRNA_{comK}]}{dt} = k_1[P^{const}_{comK}] + f(K, k_2, k_k, n)[P_{comK}] - k_7 \cdot [mRNA_{comK}], \quad (2.3)$$

$$\frac{d[mRNA_{comS^*}]}{dt} = k_4[P^{const}_{comS^*}] + g(K, k_5, k_s, p, S^*, b_{ss}, s_s, n^*)[P_{comS^*}] - k_9 \cdot [mRNA_{comS^*}], \quad (2.4)$$

$$\frac{d[ComK]}{dt} = k_3 \cdot [mRNA_{comK}] - k_8[ComK] - k_{11} \cdot [MecA] \cdot [ComK] + k_{-11}[MecA_K], \quad (2.5)$$

$$\frac{d[ComS^*]}{dt} = k_6 \cdot [mRNA_{comS^*}] - k_{10}[ComS^*] - k_{13} \cdot [MecA] \cdot [ComS^*] + k_{-13}[MecA_S], \quad (2.6)$$

$$\frac{d[MecA_K]}{dt} = k_{11} \cdot [MecA] \cdot [ComK] - k_{-11}[MecA_K] - k_{12}[MecA_K], \quad (2.7)$$

$$\frac{d[MecA_S]}{dt} = k_{13} \cdot [MecA] \cdot [ComS^*] - k_{-13}[MecA_S] - k_{14}[MecA_S]. \quad (2.8)$$

2.3.2 Bifurcation Analysis

We studied the dynamics of the 6-ODE continuous description of CircuitOne with sufficient timescale separation between protein expression and mRNA dynamics. Figure 2.1(A) shows the bifurcation analysis [29, 30, 31, 32] of the 6-ODE model as a function of bs^*, the coupling strength at the intermediate gene, in the otherwise negative regulation loop of CircuitOne. SN refers to the saddle-node bifurcation at $bs^* = 42.4$, which corresponds to a collision between two fixed points: a saddle and a stable node; HB refers to the subcritical Hopf bifurcation at $bs^* = 419.6$, at which the stability of the fixed points changes from unstable to stable. At the Hopf point, an unstable limit cycle is born and this is indicated by red dashed lines emanating from the bifurcation point. An unstable limit cycle (also sometimes loosely called an unstable periodic "orbit") is a loop in the dynamical phase plane, from which the local vector field always points away. As the coupling strength bs^* is further increased, the unstable limit cycle grows until $bs^* = 1696$ where it collides with the already existing stable limit cycle (red solid line) at the cyclic fold (CF) bifurcation. HC refers to the saddle-homoclinic bifurcation at $bs^* = 5.9$ where the stable periodic orbit is lost due to the collision of the stable periodic orbit passing through the saddle. Figure 2.1(A)

shows the maximum and minimum values of the stable and unstable limit cycles as red solid and dashed lines, respectively. At the CF bifurcation point, the periodic oscillatory dynamics therefore disappears: the unstable orbit collides with the stable one to "annihilate" each other. The 6-ODE model is closer to the stochastic model. As expected, the thermodynamic limit of the stochastic model with high free MecA, agrees with the 6-ODE model.

2.4 The 2-ODE Deterministic Model

2.4.1 Model Description

Considering Eq. (2.3) and assuming that the concentration of $[mRNA_{comK}]$, i.e., the number of $mRNA_{comK}$, is constant, we get

$$0 = \frac{d[mRNA_{comK}]}{dt} = k_1[P_{comK}^{const}] + f(K, k_2, k_k, n)[P_{comK}] - k_7 \cdot [mRNA_{comK}].$$

So,

$$[mRNA_{comK}] = \frac{k_1[P_{comK}^{const}]}{k_7} + \frac{f(K, k_2, k_k, n)[P_{comK}]}{k_7}. \tag{2.9}$$

Considering Eq. (2.4) and assuming that the concentration of $[mRNA_{comS^*}]$, i.e., the number of $mRNA_{comS^*}$, is constant, we get

$$0 = \frac{d[mRNA_{comS^*}]}{dt} = k_4[P_{comS^*}^{const}] + g(K, k_5, k_s, p, S^*, b_{ss}, s_s, n^*)[P_{comS^*}] - k_9 \cdot [mRNA_{comS^*}].$$

So,

$$[mRNA_{comS^*}] = \frac{k_4[P_{comS^*}^{const}]}{k_9} + \frac{g(K, k_5, k_s, p, S^*, b_{ss}, s_s, n^*)[P_{comS^*}]}{k_9}. \tag{2.10}$$

Considering Eq. (2.7) and assuming that the concentration of $[MecA_K]$, i.e., the number of $MecA_K$, is constant, we get

$$0 = \frac{d[MecA_K]}{dt} = k_{11} \cdot [MecA] \cdot [ComK] - k_{-11}[MecA_K] - k_{12}[MecA_K].$$

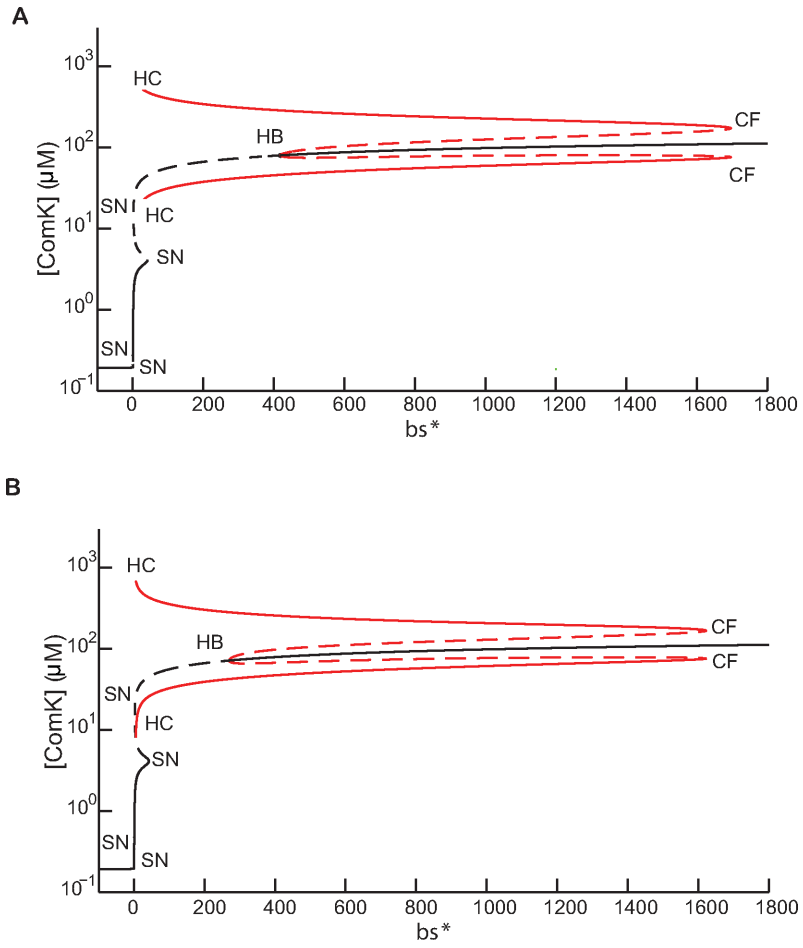

Figure 2.1. **Bifurcation diagram of the 6-ODE model and of the adiabatic 2-ODE model. (A)** Bifurcation diagram of the 6-ODE model with respect to parameter bs^*. The black curves represent the fixed points and the red curves represent the limit cycles, solid for stable and dashed for unstable. The system has saddle-node (SN), subcritical Hopf (HB), saddle-homoclinic (HC) and cyclic fold (CF) bifurcations. At the HB, the focus changes from unstable to stable with bs^* increasing. An unstable limit cycle (red dashed curve) is born at HB and annihilates the circumventing stable limit cycle (red solid curve) at the bifurcation point CF. With bs^* decreasing, the stable limit cycle vanishes as it collides with the saddle at HC. The parameters [23, 33] are shown in Table 2.3.2. **(B)** Bifurcation diagram of the adiabatic 2-ODE model with respect to parameter bs^*. The meaning of the curves and points are similar to those in (A), and the bifurcation structure of the reduced 2-ODE model is similar to that of the 6-ODE model. The parameters are shown in in Table 2.3.2.

Table 2.1. Parameter Set for 6-ODE Model

$k_1(s^{-1})$	$k_2(s^{-1})$	$k_3(s^{-1})$	$k_4(s^{-1})$	$k_5(s^{-1})$	$k_6(s^{-1})$
0.00525	4.5	0.2	2.4×10^{-4}	0.036	0.2
$k_7(s^{-1})$	$k_8(s^{-1})$	$k_9(s^{-1})$	$k_{10}(s^{-1})$	$k_{11}(nM^{-1}s^{-1})$	$k_{-11}(s^{-1})$
0.05	1×10^{-5}	0.05	1×10^{-5}	2.02×10^{-5}	11.62
$k_{12}(s^{-1})$	$k_{13}(nM^{-1}s^{-1})$	$k_{-13}(s^{-1})$	$k_{14}(s^{-1})$	$k_k(nM)$	$k_s(nM)$
0.5	4.5×10^{-5}	0.0212	4×10^{-4}	1.2×10^5	2×10^4
n	p	$s_s(nM)$	n^*	$P_{comK}^{const}(nM)$	$P_{comK}(nM)$
2	5	96	2	1	1
$P_{comS}^{const}(nM)$	$P_{comS}(nM)$	$MT(nM)$	b_{ss}	b_{s^*}	—
1	1	120	400	1200	—

Table 2.2. Parameter Set for 2-ODE Model

α_k	β_k	δ_k	λ_k	k_k	Γ_k	Γ_s	n
8.54×10^{-4}	0.6	1×10^{-4}	1×10^{-5}	4×10^3	2×10^4	16	2
α_s	β_s	δ_s	λ_s	k_s	s_s	n^*	p
3.2×10^{-5}	8×10^{-3}	1×10^{-4}	1×10^{-5}	666.6667	3.2	2	5

So,

$$[MecA_K] = \frac{k_{11} \cdot [MecA] \cdot [ComK]}{k_{-11} + k_{12}}. \tag{2.11}$$

Considering Eq. (2.8) and assuming that the concentration of $[MecA_S]$, i.e., the number of $MecA_S$, is constant, we get

$$0 = \frac{d[MecA_S]}{dt} = k_{13} \cdot [MecA] \cdot [ComS^*] - k_{-13}[MecA_S] - k_{14}[MecA_S].$$

So,

$$[MecA_S] = \frac{k_{13} \cdot [MecA] \cdot [ComS^*]}{k_{-13} + k_{14}}. \tag{2.12}$$

Because the total concentration of $[MecA]$, $[MecA_K]$ and $[MecA_S]$, denoted by $[M_T]$, is constant, we get

$$\begin{aligned} [M_T] &= [MecA] + [MecA_K] + [MecA_S] \\ &= [MecA] + \frac{k_{11} \cdot [MecA] \cdot [ComK]}{k_{-11} + k_{12}} + \frac{k_{13} \cdot [MecA] \cdot [ComS^*]}{k_{-13} + k_{14}}. \end{aligned} \tag{2.13}$$

So,

$$[MecA] = \frac{[M_T]}{1 + \frac{k_{11} \cdot [ComK]}{k_{-11} + k_{12}} + \frac{k_{13} \cdot [ComS^*]}{k_{-13} + k_{14}}}. \tag{2.14}$$

Now, we consider Eq. (2.5):

$$
\begin{aligned}
\frac{d[ComK]}{dt} &= k_3 \cdot [mRNA_{comK}] - k_8[ComK] - k_{11} \cdot [MecA] \cdot [ComK] \\
&\quad + k_{-11}[MecA_K] \\
&= k_3 \cdot \left(\frac{k_1[P_{comK}^{const}]}{k_7} + \frac{f(K, k_2, k_k, n)[P_{comK}]}{k_7} \right) \\
&\quad - k_8[ComK] \\
&\quad - k_{11} \cdot [MecA] \cdot [ComK] \\
&\quad + k_{-11} \frac{k_{11} \cdot [MecA] \cdot [ComK]}{(k_{-11} + k_{12})} \\
&= \frac{k_1 k_3 [P_{comK}^{const}]}{k_7} \\
&\quad + \frac{k_3 f(K, k_2, k_k, n)[P_{comK}]}{k_7} \\
&\quad - k_{11} \cdot [MecA] \cdot [ComK] \cdot \left(1 - \frac{k_{-11}}{k_{-11} + k_{12}} \right) \\
&\quad - k_8[ComK] \\
&= \frac{k_1 k_3}{k_7} \cdot [P_{comK}^{const}] \\
&\quad + \frac{k_3}{k_7} \cdot \frac{k_2 K^n}{k_k^n + K^n} \cdot [P_{comK}] \\
&\quad - \frac{[M_T]}{1 + \frac{k_{11} \cdot [ComK]}{k_{-11} + k_{12}} + \frac{k_{13} \cdot [ComS^*]}{k_{-13} + k_{14}}} \cdot [ComK] \cdot \frac{k_{11} k_{12}}{k_{-11} + k_{12}} \\
&\quad - k_8[ComK] \\
&= \frac{k_1 k_3}{k_7} \cdot [P_{comK}^{const}] \\
&\quad + \frac{k_2 k_3}{k_7} \cdot [P_{comK}] \cdot \frac{K^n}{k_k^n + K^n} \\
&\quad - \frac{k_{11} k_{12} [M_T]}{k_{-11} + k_{12}} \cdot \frac{[ComK]}{1 + \frac{k_{11}[ComK]}{k_{-11} + k_{12}} + \frac{k_{13}[ComS^*]}{k_{-13} + k_{14}}} \\
&\quad - k_8[ComK] \\
&= \alpha_k + \frac{\beta_k K^n}{k_k^n + K^n} - \frac{\delta_k K}{1 + \frac{K}{\Gamma_k} + \frac{S^*}{\Gamma_s}} - \lambda_k K, \qquad (2.15)
\end{aligned}
$$

where

$$K = [ComK], \tag{2.16}$$

$$\alpha_k = \frac{k_1 k_3}{k_7} \cdot [P_{comK}^{const}] = \frac{k_1 k_3}{k_7} \cdot \frac{P_{comK}^{const}}{\Omega}, \tag{2.17}$$

$$\beta_k = \frac{k_2 k_3}{k_7} \cdot [P_{comK}] = \frac{k_2 k_3}{k_7} \cdot \frac{P_{comK}}{\Omega}, \tag{2.18}$$

$$\delta_k = \frac{k_{11} k_{12} [M_T]}{k_{-11} + k_{12}}, \tag{2.19}$$

$$\Gamma_k = \frac{k_{-11} + k_{12}}{k_{11}}, \tag{2.20}$$

$$\Gamma_s = \frac{k_{-13} + k_{14}}{k_{13}}, \tag{2.21}$$

$$\lambda_k = k_8. \tag{2.22}$$

Similarly, we consider Eq. (2.6):

$$
\begin{aligned}
\frac{d[ComS^*]}{dt} &= k_6 \cdot [mRNA_{comS^*}] - k_{10}[ComS^*] - k_{13} \cdot [MecA] \cdot [ComS^*] \\
&\quad +k_{-13}[MecA_S] \\
&= k_6 \cdot \left(\frac{k_4[P^{const}_{comS^*}]}{k_9} + \frac{g(K, k_5, k_s, p, S^*, b_{ss}, s_s, n^*)[P_{comS^*}]}{k_9} \right) \\
&\quad -k_{10}[ComS^*] \\
&\quad -k_{13} \cdot [MecA] \cdot [ComS^*] \\
&\quad +k_{-13} \frac{k_{13} \cdot [MecA] \cdot [ComS^*]}{(k_{-13} + k_{14})} \\
&= \frac{k_4 k_6 [P^{const}_{comS^*}]}{k_9} \\
&\quad + \frac{k_6 g(K, k_5, k_s, p, S^*, b_{ss}, s_s, n^*)[P_{comS^*}]}{k_9} \\
&\quad -k_{13} \cdot [MecA] \cdot [ComS^*] \cdot \left(1 - \frac{k_{-13}}{k_{-13} + k_{14}} \right) \\
&\quad -k_{10}[ComS^*] \\
&= \frac{k_4 k_6}{k_9} \cdot [P^{const}_{comS^*}] \\
&\quad + \frac{k_6}{k_9} \cdot \frac{k_5 k_s^p}{k_s^p + K^p} \cdot \frac{b_{ss} S^{*n^*}}{s_s^{n^*} + S^{*n^*}} \cdot [P_{comS^*}] \\
&\quad - \frac{[M_T]}{1 + \frac{k_{11} \cdot [ComK]}{k_{-11} + k_{12}} + \frac{k_{13} \cdot [ComS^*]}{k_{-13} + k_{14}}} \cdot [ComS^*] \cdot \frac{k_{13} k_{14}}{k_{-13} + k_{14}} \\
&\quad -k_{10}[ComS^*] \\
&= \frac{k_4 k_6}{k_9} \cdot [P^{const}_{comS^*}] \\
&\quad + \frac{k_5 k_6 b_{ss}}{k_9} \cdot [P_{comS^*}] \cdot \frac{k_s^p}{k_s^p + K^p} \cdot \frac{S^{*n^*}}{s_s^{n^*} + S^{*n^*}} \\
&\quad - \frac{k_{13} k_{14} [M_T]}{k_{-13} + k_{14}} \cdot \frac{[ComS^*]}{1 + \frac{k_{11}[ComK]}{k_{-11} + k_{12}} + \frac{k_{13}[ComS]}{k_{-13} + k_{14}}} \\
&\quad -k_{10}[ComS^*] \\
&= \alpha_s + \beta_s \frac{k_s^p}{k_s^p + K^p} \cdot \frac{S^{*n^*}}{s_s^{n^*} + S^{*n^*}} - \frac{\delta_s S^*}{1 + \frac{K}{\Gamma_k} + \frac{S^*}{\Gamma_s}} - \lambda_s S^*, \qquad (2.23)
\end{aligned}
$$

where

$$S^* = [ComS^*], \tag{2.24}$$

$$\alpha_s = \frac{k_4 k_6}{k_9} \cdot [P^{const}_{comS^*}] = \frac{k_4 k_6}{k_9} \cdot \frac{P^{const}_{comS^*}}{\Omega}, \tag{2.25}$$

$$\beta_s = \frac{k_5 k_6 b_{ss}}{k_9} \cdot [P_{comS^*}] = \frac{k_5 k_6 b_{ss}}{k_9} \cdot \frac{P_{comS^*}}{\Omega}, \tag{2.26}$$

$$\delta_s = \frac{k_{13} k_{14} [M_T]}{k_{-13} + k_{14}}, \tag{2.27}$$

$$\lambda_s = k_{10}. \tag{2.28}$$

Now, we get the dimensioned version (in the unit of nM/s):

$$\boxed{\frac{dK}{dt} = \alpha_k + \frac{\beta_k K^n}{k_k^n + K^n} - \frac{\delta_k K}{1 + \frac{K}{\Gamma_k} + \frac{S}{\Gamma_s}} - \lambda_k K}. \tag{2.29}$$

$$\boxed{\frac{dS^*}{dt} = \alpha_s + \beta_s \frac{k_s^p}{k_s^p + K^p} \cdot \frac{S^{*n^*}}{s_s^{n^*} + S^{*n^*}} - \frac{\delta_s S^*}{1 + \frac{K}{\Gamma_k} + \frac{S^*}{\Gamma_s}} - \lambda_s S^*}. \tag{2.30}$$

2.4.2 Bifurcation Analysis

Due to timescale separation, the 6-ODE continuous model can be reduced to a 2-ODE model via adiabatic approximation. Figure 2.1(B) a bifurcation diagram of the 2-ODE model with ComK vs. bs^*. SN refers to a saddle-node bifurcation at $bs^* = 42.4$. HB refers to the subcritical Hopf bifurcation at $bs^* = 270.3$, CF refers to the cyclic fold bifurcation at $bs^* = 1622$ and HC refers to a saddle-homoclinic bifurcation at $bs^* = 5.9$. We find that the bifurcation structure is similar to that of 6-ODE model shown in Figure 2.1(A). However, since in the 6-ODE system, there is only imperfect timescale separation of dynamics, the bifurcations of the 2-ODE model are located at slightly different locations. We note that the bifurcation diagrams show the presence of an unstable limit cycle, which is a circling ravine in the probability of residence. In terms of a potential function, from which the vector field on the phase

plane is derived, it can be thought of as a circling ridge. The analogy with a ridge can be formalized by establishing the correspondence of the vector field to the height of the ridge, in terms of the underlying stochasticity, via a potential function [34].

2.5 Comparison of Behaviors between 6-ODE and 2-ODE Models

2.5.1 Comparison in Phase Portrait

Figure 2.2 presents a phase plane analysis of the excitable configuration. The ComK nullcline (red) has a single branch, but the ComS* nullcline possesses multiple branches shown in cyan, yellow and green. The 6-ODE equivalent curves to the 2-ODE nullclines are shown on the 2-dimensional (ComK, ComS*)-phase plane as red dots (ComK) and black squares (ComS*). As expected, because of time-scale separation in the 6-ODE model, we find general good agreement between the 2-ODE nullclines and their 6-ODE equivalent. However, we notice that timescale separation in the 6-ODE system is not quite sufficient to yield complete and exact agreement between the 6-ODE model and its 2-ODE reduced version, throughout the entirety of the dynamics. Local discrepancy exists in the peak and the valley of the ComK nullcline. The 6-ODE ComK curve pinches upwards in the peak region and pinches downwards in the valley region. This is indicated by dashed lines connecting the red dots. In contrast, in the same regions, the 2-ODE ComK nullcline smoothly rounds out. Purple stars mark the locations of the fixed points of the 6-ODE dynamics. They correctly coincide with the intersections of the 2-ODE ComK and ComS* nullclines, thus demonstrating excellent agreement between the 2-ODE and 6-ODE descriptions, for the basic nature of the dynamics of the system.

Focusing on differences however, the magenta asterisk #4 in Figure 2.2 locates a saddle-like region of the 6-ODE dynamics. This dynamical feature does not exist

in the 2-ODE description because the 2-ODE ComK and ComS* nullclines, although coming numerically very close to each other in this region of the phase plane, do not precisely intersect. In Figure 2.2 we provide, for each fixed point of the 6-ODE dynamics, a composite speed metric ($\sqrt{(dK/dt)^2 + (dS^*/dt)^2}$) that measures the local speed of the dynamics. Thus, we see that the 6-ODE dynamics slows down considerably near canonical fixed point #1, #2 and #3. The 6-ODE dynamics slows down much less, but still appreciably, near the saddle-like feature indicated by the magenta asterisk #4. As demonstrated by the blue stochastic track, this location is exactly where the stochastic dynamics also dwells. The observed dynamical feature is explained as stochastic dwelling in the vicinity of a relatively flat 6-ODE saddle-like region of phase space. Figure 2.2 also indicates the presence of a stable node and hyperbolic fixed point in the 6-ODE dynamics. These features (node #5 and #6) are located in the lower left corner of the phase plane. The 2-ODE description does not show these dynamical features. The mismatch in dynamics is due to incomplete timescale separation in the 6-ODE model, compared to complete timescale separation in the 2-ODE model. We have verified that a saddle-node bifurcation does also occur in the 2-ODE model, but at a lower bs^* (data not shown), thus restoring the agreement in dynamics. Furthermore, we note that the region of the phase plane where the saddle-node bifurcation occurs is biologically inaccessible because it resides at ComS* below 1 molecule ([ComS*]$<$ 1nM).

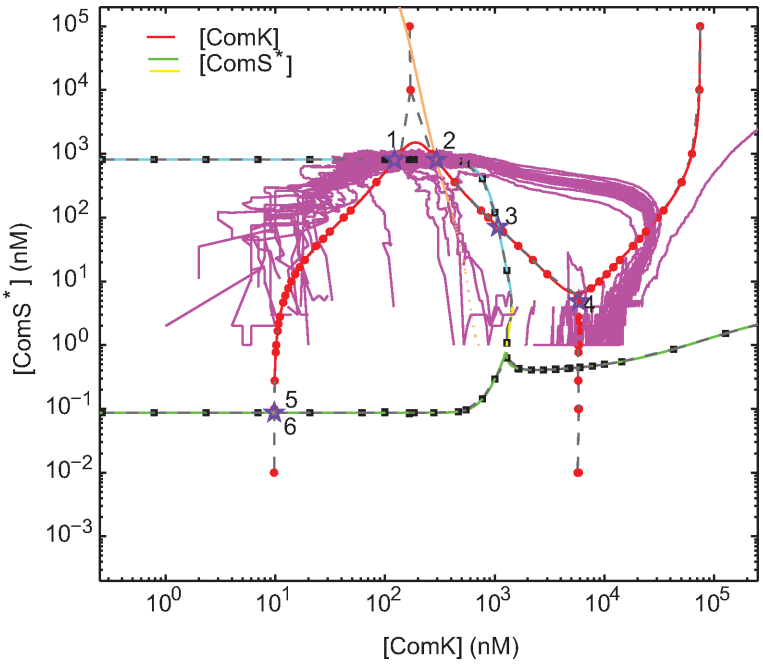

1 quasi stable node	8.31×10^{-18}
2 hyperbolic fixed point	2.09×10^{-18}
3 unstable spiral point	7.61×10^{-18}
4 hyperbolic fixed point	9.03×10^{-5}
5 hyperbolic fixed point	2.14×10^{-6}
6 quasi stable node	2.21×10^{-6}

Figure 2.2. **Agreement of dynamics between 2-ODE and 6-ODE models at $bs^* = 5$.** The red circles depict the ComK nullcline, and the gray circles depict the ComS* corresponding equivalent curve. The solid red curves delineate the ComK nullcline and the cyan, yellow and green curves delineate the ComS* nullclines of the 2-ODE model, respectively. The magenta curves are the result from the stochastic simulation. The stability of the different points is shown in the table below the plot.

2.5.2 Comparison in Bifurcation Structure

Figure 2.1(A) and Figure 2.1(B) are similar and they naturally define three dynamical regions of interest: $bs^* <$ HB, HB $< bs^* <$CF and $bs^* >$CF. These regions have the following dynamical nature: stable limit cycle around an unstable focus, stable limit cycle around a stable focus surrounded (i.e. shielded) by a unstable limit cycle, and stable focus (spiral).

2.6 Nullclines and Fixed Points

We solve a 5-equation system to find the nullclines of ComK and ComS*, respectively, in 6D-ODE system which are equivalent to those obtained in 2D-ODE system.

To get the ComK nullclines, we solve

$$\begin{cases} \frac{d[mRNA_{comK}]}{dt} = 0 \\ \frac{d[mRNA_{comS^*}]}{dt} = 0 \\ \frac{d[ComK]}{dt} = 0 \\ \frac{d[MecA_K]}{dt} = 0 \\ \frac{d[MecA_S]}{dt} = 0 \end{cases}, \tag{2.31}$$

without considering $\frac{d[ComS^*]}{dt} = 0$. We search for the solutions grid by grid in the ComK-ComS* phase plane. For each ComS* grid, we try one by one several ComK grids in a certain range, of which some may converge to one solution, and others may converge to another solution. This is reason why there may have several branches for each nullcline (see Figure 2.3).

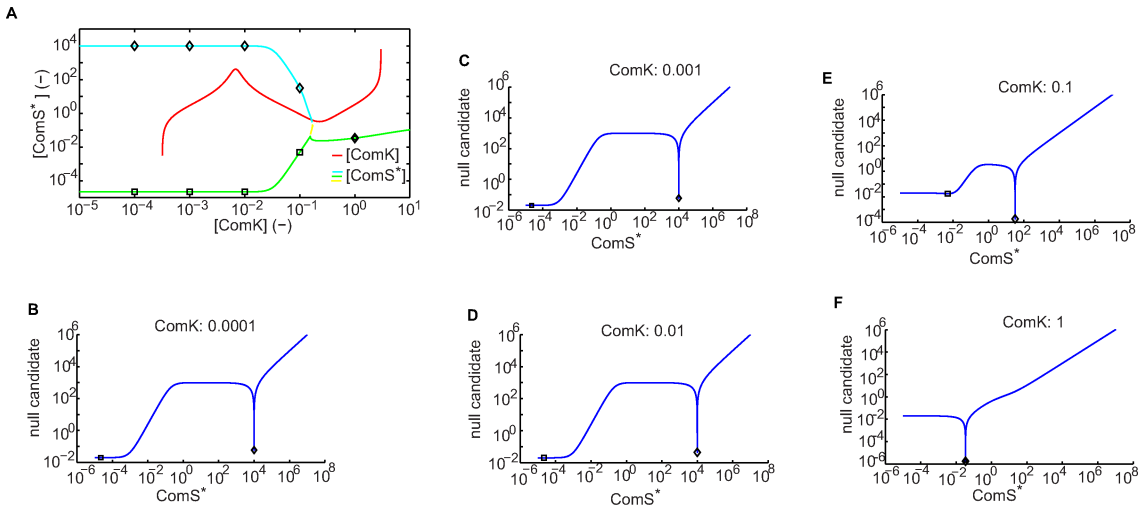

Figure 2.3. **Details of the calculation of ComS* multi-branch nullclines.** Diamonds denote the nodes in the upper branch (the larger ComS* values), and the squares denote the nodes in the lower branch (the smaller ComS* values). **(A)** The red curve is the ComK nullcline. The cyan, yellow and green curves are the ComS* multi-branch nullclines. **(B-F)** For each ComK value, we find the ComS* nullcline candidates for which the absolute dComS*/dt value falls below a threshold equal to 0.1. We then select the local minima of the candidates as the solutions.

Similarly, to get the ComS* nullclines, we solve

$$\begin{cases} \frac{d[mRNA_{comK}]}{dt} = 0 \\ \frac{d[mRNA_{comS*}]}{dt} = 0 \\ \frac{d[ComS^*]}{dt} = 0 \\ \frac{d[MecA_K]}{dt} = 0 \\ \frac{d[MecA_S]}{dt} = 0 \end{cases}, \tag{2.32}$$

without considering $\frac{d[ComK]}{dt} = 0$, and use the same grid-by-grid searching strategy.

To get the fixed points in 6D-ODE system, we solve the 6-equation system:

$$\begin{cases} \frac{d[mRNA_{comK}]}{dt} = 0 \\ \frac{d[mRNA_{ComS^*}]}{dt} = 0 \\ \frac{d[ComK]}{dt} = 0 \\ \frac{d[ComS^*]}{dt} = 0 \\ \frac{d[MecA_K]}{dt} = 0 \\ \frac{d[MecA_S]}{dt} = 0 \end{cases} . \tag{2.33}$$

The scheme is also to search grid-by-grid for solutions in the given range of ComK-ComS* phase space. We calculate the eigenvalues of 6×6 Jacobian matrix and determine the types of the fixed points based on the relationships of all 6 eigenvalues [35].

It is noticed that the solutions approach to zero with different orders of magnitude, which may correspond to their potential gradients or the residency probabilities.

The 2D-ODE nullclines, equivalent ones obtained in 6D-ODE system and fixed points are shown in Figure 2.2.

We notice that the 4-th fixed point is not exactly on the intersection of ComK and ComS* nullclines. It is due to its relatively high speed, compared with other fixed points. In the stochastic simulation there is a minor dwelling around this "quasi" hyperbolic fixed point.

Below the 4-th fixed point there is an intersection of ComK and ComS* nullclines, but no label of the fixed point is shown. In fact, there are solutions detected around the intersection, but all of them are abandoned because each solution contains negative values of the concentrations, which is not biologically meaningful.

2.7 Stochastic Search

When we plot the nullclines, if the nullclines are not ideal, e.g., not in the biologically meaningful region, we usually have to modify a set of parameters by trial and error until we get an acceptable one, if we are lucky enough.

Here, we managed to obtain the optimal parameters using a stochastic searching method based on the simulated annealing (SA) algorithm (see Figure 2.4).

2.7.1 Simulated Annealing (SA) algorithm

SA algorithm is a heuristic Monte Carlo method frequently used in the global optimization. The globally optimal solution can be achieved without solving the derivative of the objective function or a big array of equations.

The implementation of the algorithm is relatively easy, but usually time-consuming.

The workflow of the Metropolis SA algorithm [36, 37] is followed:

1. Given the variation range for each parameter of the model, select the initial parameter set, $\mathbf{m}_0$, and calculate the corresponding objective function value, $E(\mathbf{m}_0)$.
2. Generate a new parameter set, $\mathbf{m}$, by perturbating the current parameter set, $\mathbf{m}_0$; calculate the corresponding objective function value, $E(\mathbf{m})$, and get $\Delta E = E(\mathbf{m}) - E(\mathbf{m}_0)$.
3. If $\Delta E < 0$, then the probability of acceptance $p = 1$, otherwise $p = \exp(-\Delta E/T)$, where T is the temperature. Generate a pseudorandom value r drawn from the standard uniform distribution on the open interval $(0, 1)$. If $p > r$, then the new parameter set $\mathbf{m}$ is accepted, and set $\mathbf{m}_0 = \mathbf{m}$, $E(\mathbf{m}_0) = E(\mathbf{m})$.
4. At the temperature T, repeat step 2 and 3 for several rounds.
5. Gradually lower the temperature T.
6. Repeat step 2-5 until the convergence condition is satisfied.

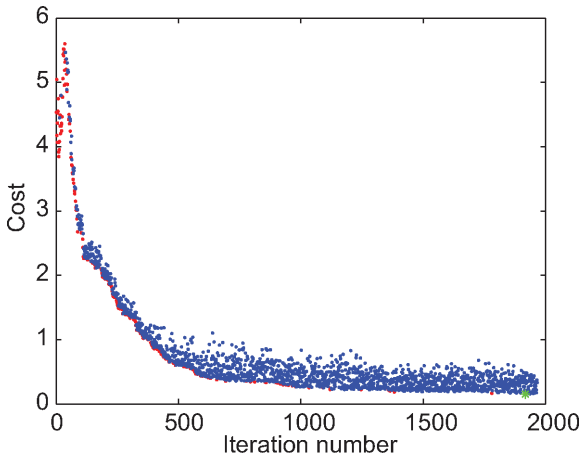

Figure 2.4. **Plot of stochastic search using SA algorithm.** Red spots correspond to the locally optimal solutions, blue spots correspond to the accepted solutions in Metropolis sense, and the green star corresponds to the globally optimal solution.

2.8 Calculation of Time in Competence (TIC)

To analyze data in a uniform way, we exclude the head and the tail of a data series such that the truncated data all start from the first trough of the oscillations. To remove some extremely high peaks, we first detect all the peaks in the data, and calculate the mean and standard deviation of the peaks, called μ_{peak} and σ_{peak}, respectively. If the absolute difference between a peak and μ_{peak} is less than $3\sigma_{peak}$, the peak is accepted, otherwise rejected. The tallest peak, $peak_0$, in the remaining "normal" peaks is selected for normalization.

CHAPTER 3

RESULTS AND DISCUSSIONS

3.1 Results

3.1.1 Behavior in the Excitable Regime

Excitability is a desired feature for the competence phenotype because it allows random duration of competence occurring at random times. This was shown to be an optimal evolutionary design feature [24] since it permits optimal sampling of a randomly changing growth and living environment of the organism.

In Figure 3.1 we show the dynamical portrait at $bs^* = 5$, just below the saddle-homoclinic bifurcation. In this regime the system is excitable. In blue we show tracks resulting from the integration of the 2-ODE system started at different initial conditions. In magenta, we show one stochastic simulation of a track falling into the stable node (#1). We note that the biochemical noise in the system is not sufficient to cause the trajectory to exit the basin of attraction of fixed point (#1). Therefore, although this regime is excitable, it does not promote competence excursions.

We combine two methods to make an excitable system excited: one is to reduce the distance between the stable node and the separatrix, and the other is to increase the intrinsic noise by reducing the number of molecules of MecA.

First, we elevated the plateau of the ComS* nullcline by increasing parameter "α_k" by 22%. This results in an intersection of the ComS* and ComK nullclines to occur at higher ComS*, in the narrower part of the ComK peak, thus nearer to the ComK maximum. For fixed level of intrinsic noise, a shorter distance (along

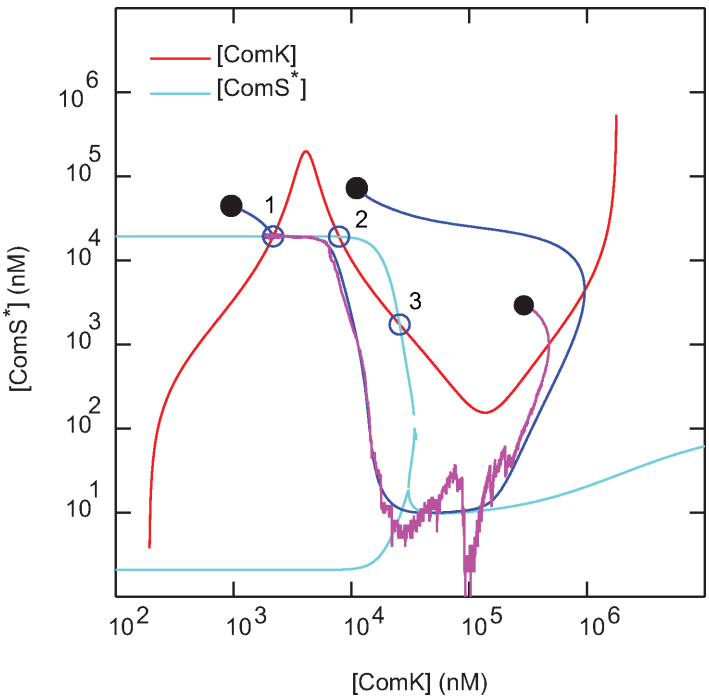

Figure 3.1. **Dynamical portrait at $bs^* = 5$, just below the saddle-homoclinic bifurcation.** Parameter sets are the same as those in Figure 2.1(A). Point #1, #2 and #3 are stable node, saddle and unstable focus, respectively. The magenta curve is a stochastically simulated trajectory falling into the stable node #1, and the two blue curves are obtained by integration of the 2-ODE system starting at different initial points.

the ComK axis) from fixed point (#1) to reach the separatrix promotes entry into competence.

Second, we set the MecA initial conditions to 3, 1, 1 molecules (for the free MecA, and the complexes of MecA with ComK or with ComS*: MecA_ComK and MecA_ComS*). Compared to 100, 10, 10 molecules used in other simulations (e.g., Figure 3.1), these lower free and complexed MecA initial conditions move the system to a lower region in the (ComK, ComS*) phase plane. This results in an increase of the intrinsic noise, particularly in ComK because ComK is already approximately an order of magnitude lower than ComS*.

The combined effect of the two methods makes an excitable system excited because it lowers the threshold and raises the noise level.

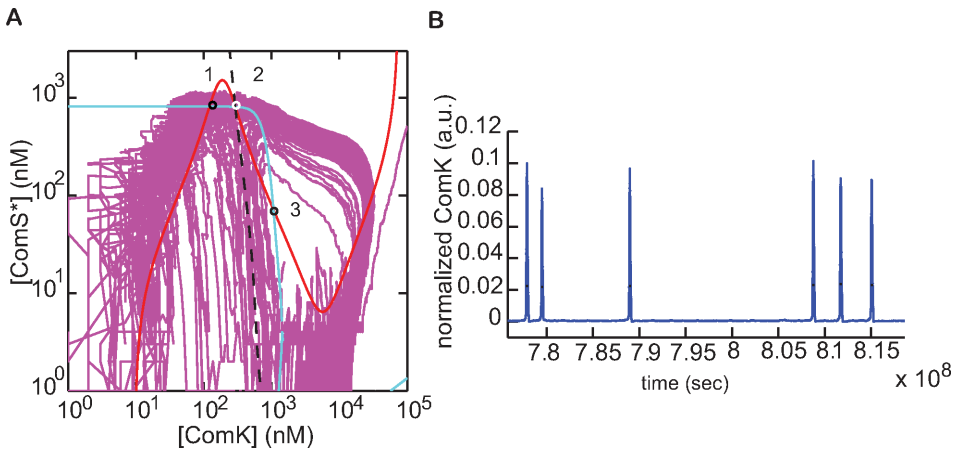

Figure 3.2. **Pure Excitability exists near the saddle-homoclinic bifurcation.** **(A)** Excitable trajectory (magenta) in the stochastic model is shown in the 2-D phase plane. The separatrix (black dashed line) between stable fixed points #1 and #3, the ComS* (cyan) and the ComK (red) nullclines of 2-ODE model are plotted in the phase plane. Point #1 refers to the stable node, #2 the saddle and #3 the unstable focus. **(B)** Excerpt of the time series from (A) shows "bursting" behavior.

In Figure 3.2(A), we show the result of increasing the intrinsic noise to promote excursions beyond the boundary of the basin of attraction of fixed point (#1). This boundary is called the separatrix. It is shown in dashed line. In the excitable case, the system possesses a stable node (#1), a saddle (#2) and an unstable focus (#3). If the initial point of the trajectory is on the right side of the separatrix, then this will result in an immediate large excursion causing the trajectory to travel around the unstable focus, and back into stable node (#1). If the initial point is on the left side of the separatrix, and if the noise is large enough, the trajectory will dwell for some time until it "escapes" from the basin of attraction of the stable node. It will then be traveling beyond the unstable saddle, and around the unstable focus, to head

back to the attractive fixed point (#1). Then the process may start again, causing another large excursion. In this way, the time series exhibits a kind of "bursting" behavior, as shown in Figure 3.2(B).

3.1.2 Behavior in the Oscillatory Regime

At $bs^* = 419.6$, (6-ODE), a subcritical Hopf (HB) bifurcation occurs. There, an unstable limit cycle is born initially with zero amplitude, and quickly grows as bs^* is increased to eventually collide and "annihilate" with the encircling stable limit cycle at the Cyclic Fold (CF, $bs^* = 1696$, 6-ODE) bifurcation.

3.1.2.1 Butterfly Mixing Effect

Figure 3.3 shows a stochastic simulation run at $bs^* = 350$, below the HB. In this region, the continuous dynamics presents stable oscillations about an unstable focus (see Figure 2.1(A)); thus we observe a stable limit cycle. The key feature that stochasticity imparts is mixing about that stable orbit. This mixing shows systematics however, and is not completely random. The noise in the upper part of the limit cycle is insufficient to cause transitions between the inner and outer regions of the stable limit cycle. Interestingly, at the bottom of the oscillations, the molecular numbers are smaller and stochastic variations of sufficient size occur causing stochastic mixing about the stable limit cycle. The stochastic system therefore has a tendency to orbit the upper part of the stable limit cycle on one side (inner or outer), mix in the lower region, and transit the orbit on the other side (outer or inner) of the stable limit cycle. We dubbed this crisscrossing effect "Butterfly Mixing".

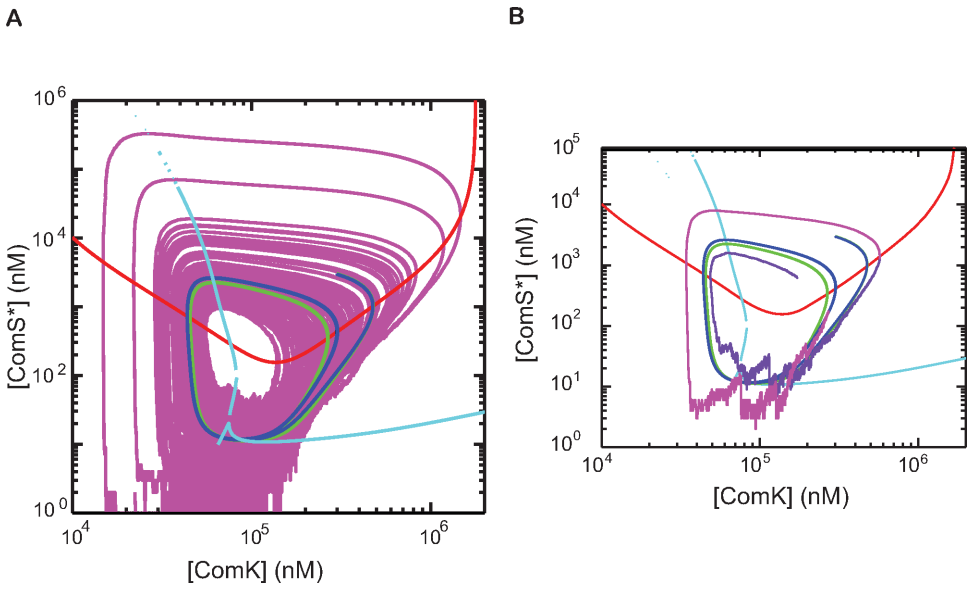

Figure 3.3. **The "Butterfly Mixing" effect. (A)** Stochastic simulation at $bs^* = 350$. The blue and green curves are trajectories of the 6-ODE and 2-ODE model, respectively. The curve in magenta is the stochastic trajectory. **(B)** Excerpt of the stochastic trajectory shows the "Butterfly Mixing" effect. We switch the color of the stochastic trajectory from magenta to purple in order to clearly show where the dynamics crosses from outside to inside the stable limit cycle.

3.1.2.2 Stochastic Shield Effect

Figure 3.4(A) shows the phase portrait of the continuous dynamics at $bs^* = 500$, thus in the region beyond the Hopf (HB), but before the CF. In this region, we observe coexistence of the periodic oscillatory behavior with a shielded attractive focus. The stable focus is effectively shielded by the presence of an unstable limit cycle. That unstable limit cycle hence splits the phase space in the inner part of the stable orbit region into two sub-regions with very different dynamics. The location of the unstable limit cycle is shown in converging green spiral from the 2-ODE model. This trajectory is computed by integrating the differential equation set backwards in time.

From a radius smaller than that of the unstable limit cycle, thus within it, all trajectories travel inwards along a spiral and fall into fixed point (#1) (see Figure

3.4(B)). From outside the unstable limit cycle, but at a radius still smaller than that of the encircling stable orbit, all trajectories are attracted outward to the stable limit cycle (see Figure 3.4(A)). And, finally, from outside the stable limit cycle, dynamics is attractive everywhere to that limit cycle, as shown in Figure 3.4(A) and Figure 3.4(B). A medium length stochastic simulation is shown in magenta. The stochastic trajectory does not penetrate inside the unstable limit cycle; the attractive fixed point is therefore shielded.

Figure 3.4(C) and Figure 3.4(D) are two stochastic simulations with same free MecA=100 molecules, the first one performed at $bs^* = 500$ and the second one at $bs^* = 1000$. At high bs^*, the system is noisier, and importantly, the unstable and stable limit cycles are of comparable size so the presence of the unstable limit cycle is not felt in the stochastic dynamics. But at lower bs^*, the unstable limit cycle's associated raised potential creates a very effective barrier to the circling dynamics and, in effect, the inner region of the unstable limit cycle is shielded from entry. Trajectories repeatedly attempt and fail to "ride uphill" over the unstable limit cycle. We dubbed this effect "Stochastic Shield". Importantly, at lower bs^*, the unstable limit cycle has a much smaller size than its stable counterpart.

We have performed complementary simulations (data not shown) at other values of bs^* from 350 to 1696 (near the location of the CF) confirming the trend that, as the relative size of the unstable limit cycle to that of the stable limit cycle approaches unity at the CF, so does the relative height of the underlying potentials. In other words, stochastic shielding is most efficient when the unstable limit cycle is much smaller than the stable limit cycle; stochastic shielding becomes inefficient as the CF is approached.

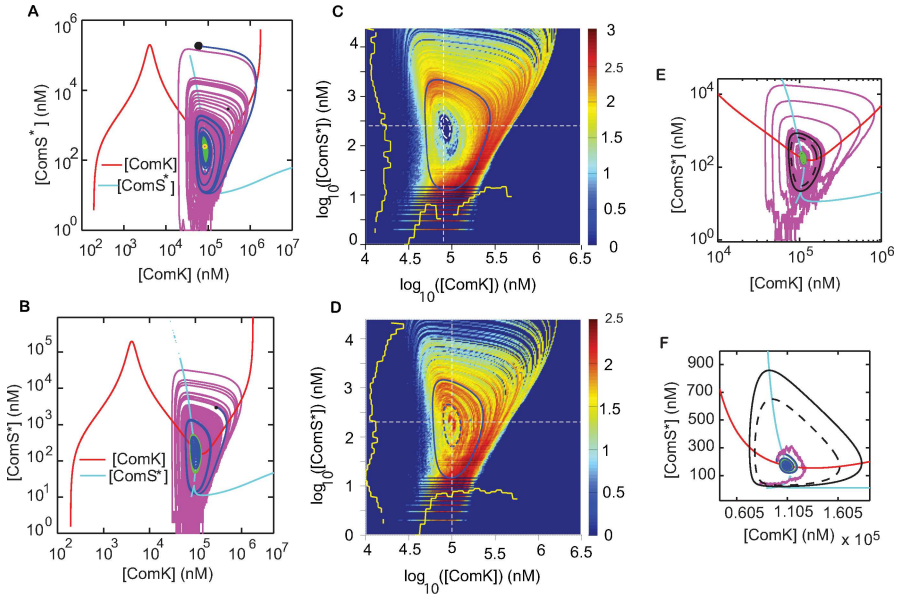

Figure 3.4. **Periodic oscillation and the effect of the unstable limit cycle. (A)** Stochastic behavior shown on the 2-ODE deterministic phase portrait at $bs^* = 500$. The deterministic system has a stable focus surrounded by an unstable limit cycle and a circumventing stable limit cycle. Two 2-ODE model trajectories shown in blue arise from different initial points in the phase plane. The green curve is the trajectory computed by integrating the differential equation set backwards in time. The stochastic trajectory (magenta) oscillates about the stable limit cycle. The values of other parameters are the same as those in Figure 2.1(A). **(B)** Stochastic behavior shown in the 2-ODE deterministic phase portrait at $bs^* = 1000$. **(C)** Residency diagram of the stochastic system at $bs^* = 500$. The stable limit cycle (solid blue loop) and the unstable limit cycle (dashed white loop) of 6-ODE model are overlaid. These orbits are circling an attractive fixed point at their center (not shown for clarity). Residency profiles are shown as yellow jagged lines. The profile at the bottom (fixed ComS*) shows the unstable limit cycle as a looping low residency trough. This is a "Stochastic Shield" because entry into the basin of attraction of the stable fixed point is prevented. **(D)** Residency diagrams of the stochastic system at $bs^* = 1000$. The unstable limit cycle is represented by the dashed blue loop. The residency profile at the bottom is generally flat. The stochastic trajectories can switch between the attractive regions of the stable focus and that of the stable limit cycle. The "Stochastic Shield" is removed. **(E)** The dynamical phase portrait at $bs^* = 1650$, slightly below the CF. The stable limit cycle is represented by the solid black loop. The unstable limit cycle is shown by a dashed black loop. **(F)** Enlargement of (E). The trajectory escapes from the basin of attraction because of noise.

3.1.2.3 Sailing Against the Wind Effect

The behavior of the system in the region between the Hopf (HB) and the Cyclic Forld (CF) is heavily influenced by the presence of the unstable limit cycle. In the biologically meaningful noise regime, the key behavior is the unintuitive stochastic escape from the attractive fixed point. An example of this behavior is shown on Figure 3.5 ($bs^* = 425$) and on Figure 3.4(E) and detailed on Figure 3.4(F) ($bs^* = 1650$). Even if the stochastic simulation is started in very close vicinity of the attractive fixed point, sufficient noise in the system makes the dynamics diverge in a characteristic way. We dubbed the manner in which the escape occurs "Sailing Against the Wind" because the stochastic system may be thought to skip from one inwardly going arc of the continuous limit trajectory to another arc, at higher radius. This behavior thus effectively counters the effect of the underlying vector field of the continuous limit model, doing it in a manner somewhat reminiscent of well-known sailing maneuver.

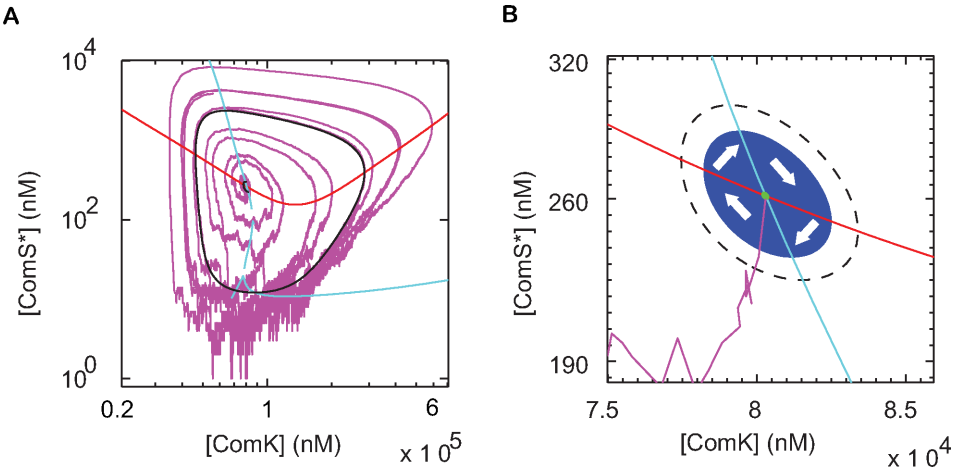

Figure 3.5. **"Sailing Against the Wind" effect.** Stochastic simulation at $bs^* = 425$. **(A)** The 6-ODE system has a stable limit cycle (the black solid loop), unstable limit cycle (small black dashed loop) and a stable focus (the green dot in (B), which is the intersection point of ComK and ComS* nucllines). The stochastic trajectory (in magenta) escapes from the basin of attraction of a stable focus due to the noise. **(B)** The enlargement near the unstable limit cycle of the (A).

To verify that the escape behavior is noise-driven, for all species in the system, we artificially increased the number of molecules and the volume of the stochastic system, keeping the ratio unchanged. Thus concentrations are the same, but as the thermodynamic limit is approached, these concentrations arise from larger numbers of molecules in a proportionally bigger volume. This condition is approximating the thermodynamic limit [28, 38]. Figure 3.6 shows the result of comparing the thermodynamic limit of the stochastic system with the 6-ODE continuous model predictions. This simulation expectedly shows that the behavior of stochastic escape from the attractive fixed point is reversed in the thermodynamic limit. Thus, in the limit of high molecular numbers and volume, with concentrations held constant, both the stochastic system and its 6-ODE continuous limit present a stable focus.

3.1.3 Behavior above the Cyclic Fold (CF)

In the 2-ODE adiabatic approximation, the encircling stable limit cycle annihilates with the inner unstable limit cycle at $bs^* = 1622$ (2-ODE model); beyond this point the dynamics should solely be driven by the presence of a single stable focus. Figure 3.7(A) shows the expected dynamics there, for the 2-ODE model. The blue track is an inwardly falling spiral to the only fixed point in the system. We note the presence of a denser region on the track (higher pitch), which we refer later as "Dwelling in Pitch". The track in magenta is the result of the stochastic simulation.

Figure 3.7(B) shows the dynamics above the CF, at $bs^* = 1700$. In this region, bifurcation analysis predicts a single attractive fixed point. The spiraling trajectory behavior just near the CF bifurcation is of high interest. Dynamics presents a region of narrower pitch, in essence the "ghost" of the previously annihilated stable limit cycle . We dubbed this "Dwelling in Pitch" effect. We observe that the "ghost" that is present for $bs^* >$ CF eventually disappears by $bs^* \approx 2000$.

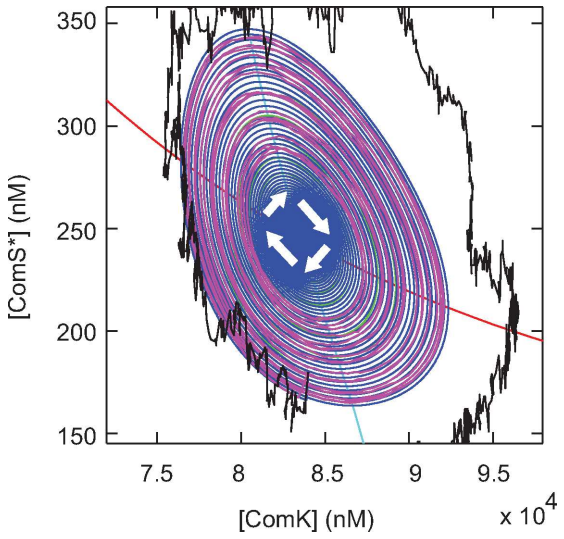

Figure 3.6. **Comparing the thermodynamic limit of the stochastic system with the 6-ODE continuous model predictions.** The "Sailing Against the Wind" effect is the noise-induced escape from the basin of attraction of the fixed point located at the intersection of the two nullclines. Here we show the effect at $bs^* = 500$. The white arrows show the direction of rotation. The vector field (not shown for clarity) of the continuous 6-ODE model develops an inwardly spiraling trajectory (blue). Due to noise, the stochastic trajectory (black) systematically escapes from the basin of attraction. This behavior is reversed in the thermodynamic limit (magenta, high molecular numbers and volume held in fixed ratio). The agreement between the 6-ODE model and the stochastic model is recovered.

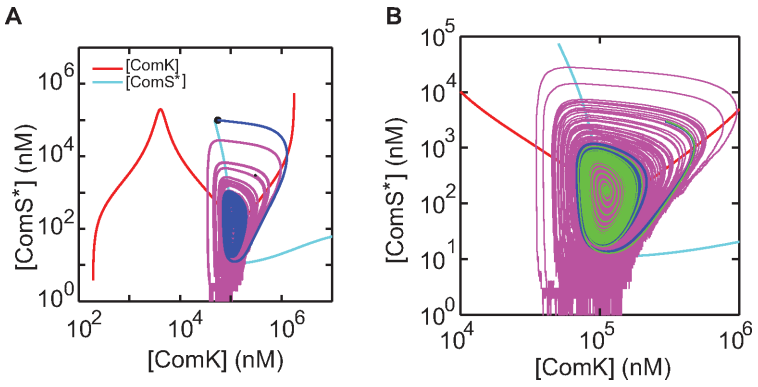

Figure 3.7. **Stochastic dynamic behavior above the cyclic fold bifurcation. (A)** Stochastic behavior is shown in the 2-ODE deterministic phase portrait at $bs^* = 1700$, just slightly above the CF. **(B)** The "Dwelling in Pitch" phenomenon in the 2-ODE phase plane at $bs^* = 1700$, just slightly after the disappearance of the stable limit cycle. The trajectory in green results from the 6-ODE model prediction.

3.1.4 Probability of Entering Competence

One of the main measures for the phenotype of competence is the probability of initiation of competence excursions. The standard way of defining this quantity is in terms of a mean waiting time to transition. Thus we define the probability of entering competence for a long trajectory going in and out of competence repeatedly, as the ratio of the total number of completed excursions into competence during the course of that trajectory, divided by the sum of time spent outside of competence, i.e. the total waiting time to transitions in the process. Furthermore, we divide by the cell cycle time for normalization. Figure 3.8 shows this quantity versus bs^* statistically. The general trend is decreasing as bs^* increases.

3.1.5 Stochastic Trap Effect

In the region between the Hopf (HB) and the Cyclic Fold (CF) bifurcations, the dynamics of the system presents an unstable limit cycle coexisting with a large encircling stable limit cycle. The unstable limit cycle is an especially interesting dynamical feature. The most intuitive way to understand this feature is in terms of the underlying vector field (dComK/dt, dComS*/dt) of the continuous model. The unstable limit cycle is a loop in phase space from which the vector field always points away from. For illustration purposes, we show in Figure 3.9 how a track inwardly falls away for the unstable limit cycle, into the stable attractor located at the intersection of the ComS* and ComK nullclines. We also show how a track with slightly different initial point also falls away from the unstable limit cycle, but in an outwardly direction, towards the other attractor in the system, the encircling stable limit cycle. For completeness, we show how a track started outside the stable limit cycle also falls into that attractor.

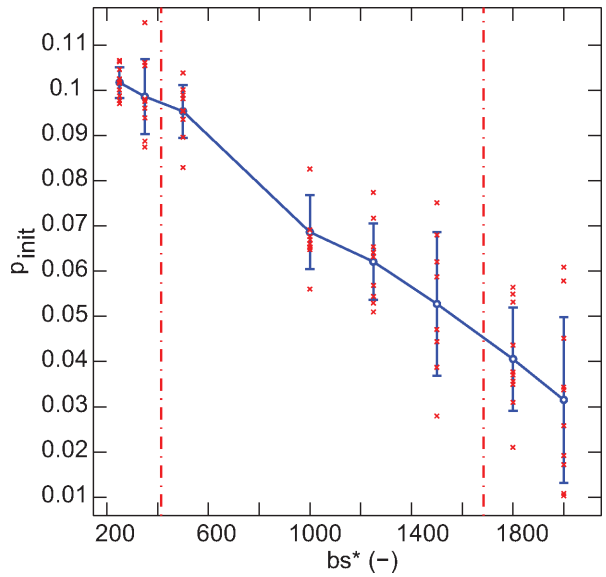

Figure 3.8. **The probability of entering competence vs. bs*.** The probability of entering competence is computed as the number of competence excursions divided by the total time out of competence, normalized to the cell cycle time. Thus, the time out of competence is a waiting time for an entry event. Entry into competence is defined as the ComK signal rising above a fixed threshold excluding rare large excursions at the 3σ level. The red dashed lines refer to two bifurcation points, left Hopf and right Cyclic Fold. As the time out of competence increases with bs^*, the probability of initiation decreases. The error bar was obtained from several statistically independent repeats at each bs^*. Because the simulation time is much larger than the cell cycle time, this plot represents the behavior of an ensemble (population) of cells.

In terms of the stochastic model, the unstable limit cycle is a loop of zero residency, in a residency diagram of ComS* vs. ComK. If the system is started on the unstable limit cycle, it will move away, either inwards or outwards, but always towards an attractor. Figure 3.10(B) displays a stochastic simulation in presence of high free MecA. High free MecA results in lower noise in the system, because the entire system dynamics is shifted upwards to higher values of ComK and ComS*. Entry into and exit from the inner region of the unstable limit cycle occur on a stochastic basis. If entry occurs, dwelling inside the unstable limit cycle for some period of time is favored; therefore the dynamics is confined to inside the unstable limit cycle.

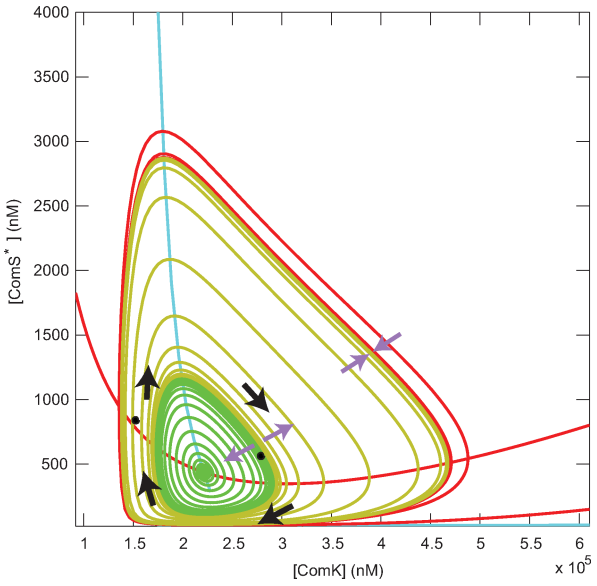

Figure 3.9. **The gradient plus curl effect.** Vector field of 2-ODE model at $bs^* = 1000$. The system has a stable limit cycle, an unstable limit cycle and a stable focus. The magenta arrows show the gradient effect, while the black arrows show the curl effect. Within the unstable limit cycle all trajectories fall into the stable focus, and outside the unstable limit cycle all trajectories fall into the stable limit cycle. In effect, the stable focus and the stable limit cycle provide a variation of the common bistable system which contains two stable fixed points.

We dubbed this effect a "Stochastic Trap". The time series of the stochastic trap is shown in Figure 3.10(A). In Figure 3.10(C), we show a similar simulation but a condition of low free MecA, which shifts the entire dynamics to lower values of ComK and ComS*, and results in higher noise in the system. In this regime, entry into and exit from the trap is unimpeded, i.e., the stochastic trap is removed.

To better understand the enabling of the stochastic trap, we computed the residency profiles at fixed ComK and ComS*. As shown in Figure 3.10(B) and Figure 3.10(C), these profiles clearly show the edges of the unstable limit cycle in the high MecA simulation, whereas the presence of the unstable limit cycle in the high noise simulation is hardly visible. The profile in Figure 3.10(C), is essentially flat and the profile in Figure 3.10(B) traces out the "canyons" of low residency of the unstable

limit cycle. The unstable limit cycle can be seen as a looping ridge of an associated potential function, both in the continuous limit of the model [39] and in the stochastic model [40]. A high potential corresponds to a low residency: the dynamics is unlikely to visit near or at the exact location of the unstable limit cycle and trajectories fall away from the unstable limit cycle in either directions: inwardly towards the stable fixed point, or outwardly towards the stable limit cycle.

Stochastic trapping of the competence excursions has profound implications on the phenotype. Foremost is the observation that the depth of the trap is under direct biological regulation of the organism via adjustment of the number of free MecA molecules. So, it is possible that an organism with the regulation of CircuitOne would dynamically implement stochastic trapping via adjustment of MecA. In the event that MecA remains fixed, as shown above, a trap of a definite depth is implemented. Depending on the ComK threshold for competence, trapping into competence or out-of-competence can therefore occur, for the time duration of stochastic dwelling of the dynamics inside the unstable orbit. CircuitOne regulation thus allows the organism to modify the sampling program of its environment for presence of exogenous DNA; hence stochastic trapping is a form of biological control of the competence phenotype.

3.2 Discussions

3.2.1 Importance of Added Positive Feedback

CircuitOne represents a modest modification of the wild-type (WT) MeKS model [22]. The core topology between these two circuits is similar with the exception of the added positive feedback of ComS onto itself (denoted ComS* in CircuitOne). To compare the expected dynamics in terms of the strength of the feedback parameter (bs in MeKS model and bs^* in CircuitOne), we generated the 2-ODE bifurcation

diagram of the MeKS model (see Figure 3.11). Most strikingly, and differing from the dynamics of CircuitOne, the WT regulation presents a super-critical Hopf bifurcation, rather than the sub-critical Hopf seen in CircuitOne. This leads to the one major difference between the two circuit dynamics: in WT dynamics, there is no unstable limit cycle. But there is also a significant similarity between these two models: most of the dynamical range is oscillatory. In a fair fraction of the dynamic range, the WT dynamics is mainly driven by a stable limit cycle of large amplitude, whereas the CircuitOne dynamics is not only controlled by a stable limit cycle, but also intricately regulated by an unstable limit cycle. Both models point to one common mystery: Why Nature only selects a very narrow region to obtain excitability? If the narrow excitable region is the WT feature, then the big remaining region can be viewed as pathological, which means the system is prone to be pathological, which contradicts the expectation of the robustness of Nature Design.

3.2.2 Stochastic Shield

The stochastic shield effect is understood based on a stochastic potential view of transitions between the two attractors: the stable limit cycle and the fixed point. As the control parameter bs^* is varied from mid-range towards the CF, the potential profile varies as illustrated in Figure 3.12. At lower values of bs^*, transitions from the stable limit cycle basin of attraction to that of the fixed point are less likely than the reverse, because of the difference in depth between the two wells in the system, relative to barrier to overcome: the top of the hump underlying the unstable limit cycle. Thus at lower bs^* the fixed point is shielded, entry into the inside region of the unstable limit cycle is not likely. But as bs^* is increased the situation reverses.

3.2.3 Stochastic Trap

In the trapping effect, the dynamics of the system is effectively captured inside the unstable limit cycle at low noise conditions (Figure 3.10(B) and (C)). As the noise in the system is reduced by increasing free MecA, the height of the potential hump underlying the unstable limit cycle is increased. Asymmetry in the potential profile leads to a difference between the probability of entry and exit. Exit from the region inside the unstable limit cycle is less probable than entry, because the depth of the fixed point stochastic potential well is greater than the depth of the stable limit cycle well, relative to the height of the hump between the two attractors (the unstable limit cycle). Equivalently, entry into the region inside the unstable limit cycle is more probable than exit, because the height to overcome to pass the barrier between the two attractors is less for entry, than the height to exit. Figure 3.13 shows a cartoon representation of this.

In summary, both Stochastic Trapping and Stochastic Shielding are manifestations of one single underlying principle: the presence of the unstable limit cycle between the two attractors defining a barrier of varying height to overcome.

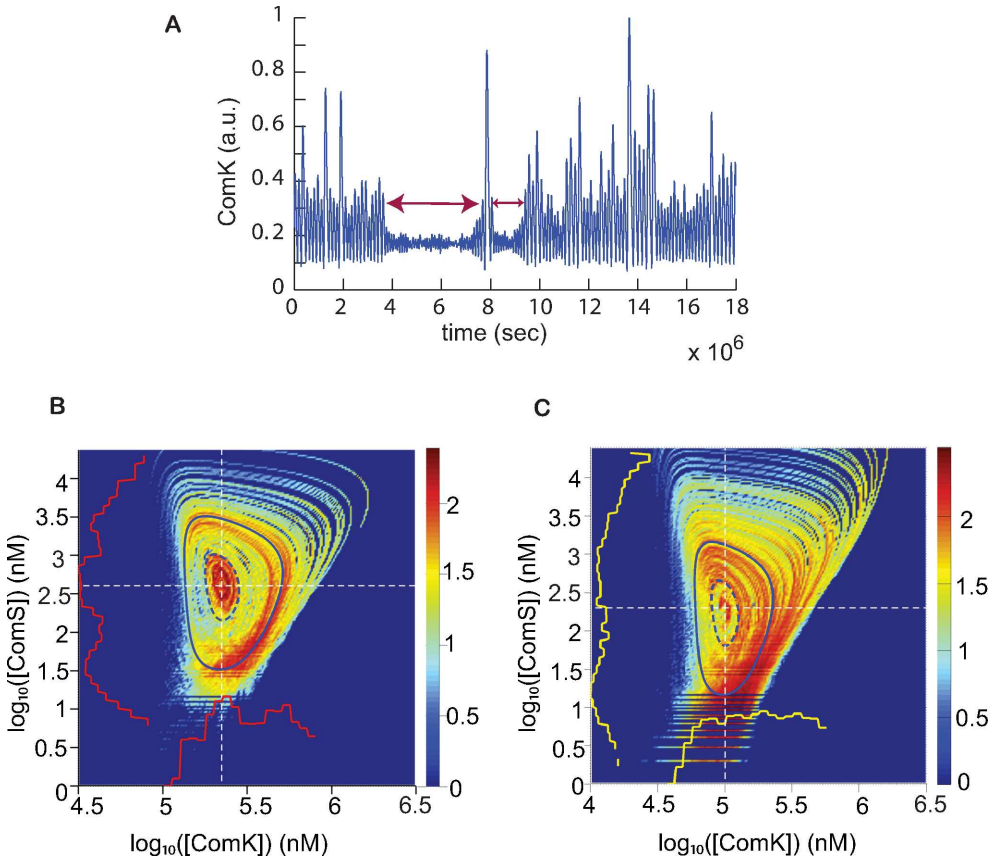

Figure 3.10. **Residency diagrams for "Stochastic Trap" effect.** **(A)** Time series at MecA= 250 nM shows the stochastic trajectory switching between two attractors, the stable fixed point and the stable limit cycle. We dubbed this effect "Stochastic Trap" Effect. **(B)** Residency diagrams at MecA= 250 nM in the phase plane of the stochastic system: two-dimensional histograms of residency as a function of the state variables ComK and ComS. Profiles in red correspond to the white dashed lines (side: fixed ComK, bottom: fixed ComS*). Peaks in the profiles aligned with the cross-hair demonstrate trapping. **(C)** Residency diagrams at MecA= 100 nM in the phase plane of the stochastic system. Profiles in yellow are flatter than (B) because of higher noise conditions. "Stochastic Trapping" is removed.

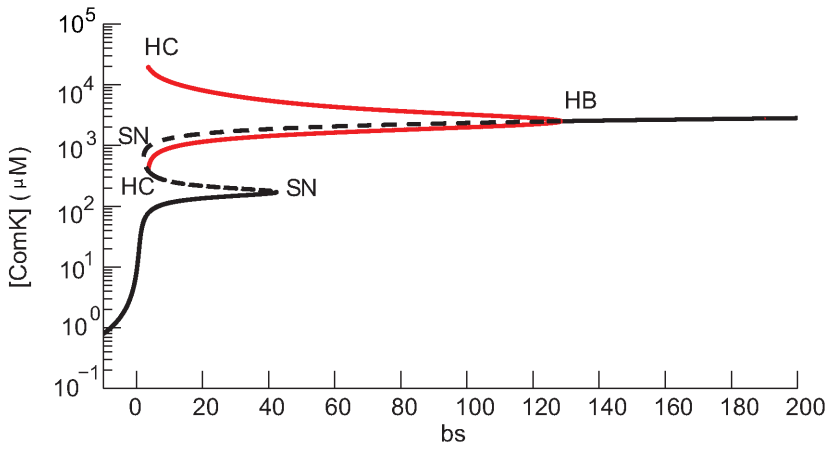

Figure 3.11. **Bifurcation diagram of MeKS model.** The values of parameters are the same as those in MeKS model, except $\alpha_s = 0.2$. We converted all the original parameters in units of nM to units of μM. HB refers to a supercritical Hopf bifurcation.

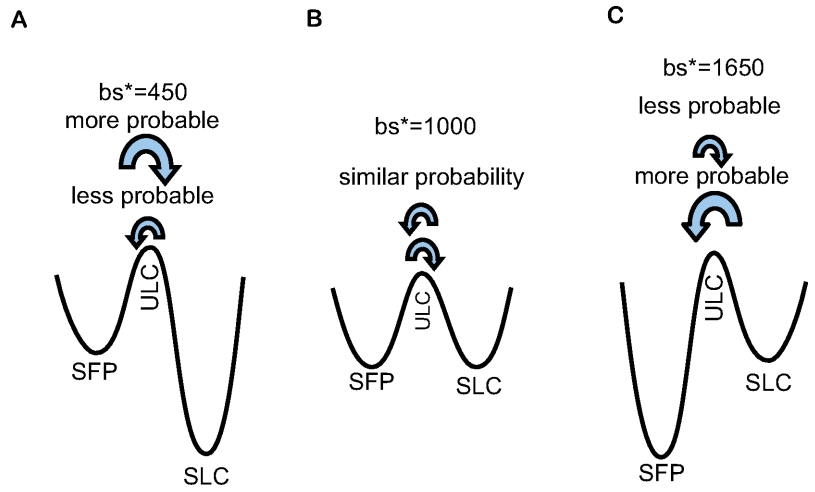

Figure 3.12. **Cartoons of the stochastic potential landscape with changing bs^*.** The stable limit cycle (SLC) and the stable fixed point (SFP) can be thought of as two potential wells. The unstable limit (ULC) cycle acts as a shield between them in the form of a hump separating the two wells. The system can be considered to be "bistable" transiting between the two dynamical attractors. **(A)** At lower bs^*, the underlying potential near the SLC is deep, and that of the SFP is shallow. **(B)** As bs^* is increased, it crosses a value ($bs^* \approx 1000$) at which the depths of the underlying potential wells are equal. **(C)** As bs^* is further increased towards the CF, the potential underlying the SFP is deeper than that underlying the SLC. Throughout, it is understood that transitions from the deep well to the shallow well are less likely than the reverse.

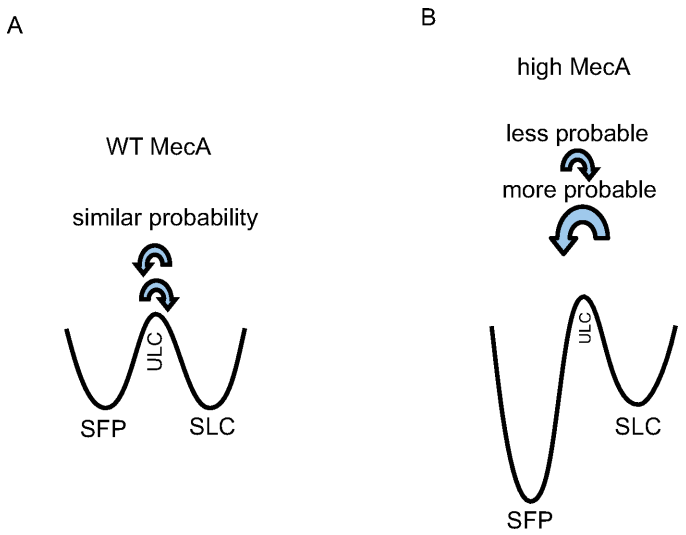

Figure 3.13. **Cartoons of the potential landscape with different levels of MecA ($bs^* = 1000$).** SFP denotes the stable fixed point, SLC the stable limit cycle, and ULC the unstable limit cycle. **(A)** Under wild-type conditions, with less MecA, the system has similar probability to fall into either the stable fixed point or the stable limit cycle. **(B)** In condition of high MecA effectively reducing the noise, the system prefers the stable fixed point to the stable limit cycle.

CHAPTER 4

CONCLUSIONS

4.1 Summary of Work

In a wide range of bs^* (see Figure 2.1) CircuitOne is a bistable system: a stable limit cycle and stable fixed point separated by an unstable limit cycle with a varying height of potential. The unstable limit cycle, together with the stable limit cycle, is shown to be critical in controlling the probability of entering competence (see Figure 3.8 for a population-level view). As bs^* increases, the unstable limit cycle inflates and the stable limit cycle deflates. The driving effect of the stable limit cycle is lessened with bs^* increasing, as the system is less and less likely to reside in the potential well of the stable limit cycle and, concomitantly, the system is more and more likely to be in the underlying well of the stable fixed point. The closer the two limit cycles, the lower the probability of entering competence. Throughout the range, the initiation probability is below the expectation value for WT *Bacillus subtilis* ($10\% \sim 25\%$, [13]). Whereas under the effect of the stable limit cycle and/or the unstable limit cycle, the probability of entering competence is generally lower than 10%.

Moreover, we have shown that the consequences of the presence of the unstable limit cycle and favorable noise conditions are profound. Through stochastic trapping (Figure 3.10) lasting at least as long as the cell cycle, CircuitOne may latch individual cells out of competence if the competence fixed point is below the threshold of competence initiation, or alternatively, latch cells into competence, if it is above. Such cells from an ensemble of cells, would be permanently competent or non-competent, for their entire lifetime.

Therefore, we conclude that as an *in silico* mutant of WT *Bacillus subtilis*, CircuitOne has less capability to accommodate the severe environmental changes, and this is probably the reason why Evolution selects the WT circuit rather than this hypothetical one.

4.2 Future Work

Our model is a high-level abstraction of the molecular mechanisms of the competence development in *Bacillus subtilis*. We make it as simple as possible and hope it to manifest the main features of cell-fate decision under the environmental stresses. And, it does provide some instructive results for experimentalists.

Next, we want to add more details to the current model so that it can take into account more events during competence development. For example, we can add quorum sensing mechanism by considering the indirect inhibition of ComS by ComK in a RapH-dependent way [1] and study the effect of ComS levels on excitability.

We also hope to extend our study to differentiation of mammalian cells, especially in a cancerous context.

REFERENCES

[1] M. Leisner, K. Stingl, E. Frey, and B. Maier, "Stochastic switching to competence," *Curr Opin Microbiol*, vol. 11, no. 6, pp. 553–9, 2008.

[2] S. V. Avery, "Cell individuality: the bistability of competence development," *Trends Microbiol*, vol. 13, no. 10, pp. 459–62, 2005.

[3] E. R. Sumner and S. V. Avery, "Phenotypic heterogeneity: differential stress resistance among individual cells of the yeast saccharomyces cerevisiae," *Microbiology*, vol. 148, no. Pt 2, pp. 345–51, 2002.

[4] M. Thattai and A. van Oudenaarden, "Stochastic gene expression in fluctuating environments," *Genetics*, vol. 167, no. 1, pp. 523–30, 2004.

[5] E. Kussell and S. Leibler, "Phenotypic diversity, population growth, and information in fluctuating environments," *Science*, vol. 309, no. 5743, pp. 2075–8, 2005.

[6] W. K. Smits, O. P. Kuipers, and J. W. Veening, "Phenotypic variation in bacteria: the role of feedback regulation," *Nat Rev Microbiol*, vol. 4, no. 4, pp. 259–71, 2006.

[7] J. J. Tyson, K. C. Chen, and B. Novak, "Sniffers, buzzers, toggles and blinkers: dynamics of regulatory and signaling pathways in the cell," *Curr Opin Cell Biol*, vol. 15, no. 2, pp. 221–31, 2003.

[8] A. Novick and M. Weiner, "Enzyme induction as an all-or-none phenomenon," *Proc Natl Acad Sci U S A*, vol. 43, no. 7, pp. 553–66, 1957.

[9] M. Cohn and K. Horibata, "Analysis of the differentiation and of the heterogeneity within a population of escherichia coli undergoing induced beta-galactosidase synthesis," *J Bacteriol*, vol. 78, pp. 613–23, 1959.

[10] S. Benzer, "Induced synthesis of enzymes in bacteria analyzed at the cellular level," *Biochim Biophys Acta*, vol. 11, no. 3, pp. 383–95, 1953.

[11] L. Cai, N. Friedman, and X. S. Xie, "Stochastic protein expression in individual cells at the single molecule level," *Nature*, vol. 440, no. 7082, pp. 358–62, 2006.

[12] M. B. Elowitz, A. J. Levine, E. D. Siggia, and P. S. Swain, "Stochastic gene expression in a single cell," *Science*, vol. 297, no. 5584, pp. 1183–6, 2002.

[13] M. G. Lorenz and W. Wackernagel, "Bacterial gene transfer by natural genetic transformation in the environment," *Microbiol Rev*, vol. 58, no. 3, pp. 563–602, 1994.

[14] D. van Sinderen, A. Luttinger, L. Kong, D. Dubnau, G. Venema, and L. Hamoen, "comk encodes the competence transcription factor, the key regulatory protein for competence development in bacillus subtilis," *Mol Microbiol*, vol. 15, no. 3, pp. 455–62, 1995.

[15] L. W. Hamoen, A. F. Van Werkhoven, J. J. Bijlsma, D. Dubnau, and G. Venema, "The competence transcription factor of bacillus subtilis recognizes short a/t-rich sequences arranged in a unique, flexible pattern along the dna helix," *Genes Dev*, vol. 12, no. 10, pp. 1539–50, 1998.

[16] R. M. Berka, J. Hahn, M. Albano, I. Draskovic, M. Persuh, X. Cui, A. Sloma, W. Widner, and D. Dubnau, "Microarray analysis of the bacillus subtilis k-state: genome-wide expression changes dependent on comk," *Mol Microbiol*, vol. 43, no. 5, pp. 1331–45, 2002.

[17] D. Dubnau, "The regulation of genetic competence in bacillus subtilis," *Mol Microbiol*, vol. 5, no. 1, pp. 11–8, 1991.

[18] D. van Sinderen and G. Venema, "comk acts as an autoregulatory control switch in the signal transduction route to competence in bacillus subtilis," *J Bacteriol*, vol. 176, no. 18, pp. 5762–70, 1994.

[19] K. Turgay, J. Hahn, J. Burghoorn, and D. Dubnau, "Competence in bacillus subtilis is controlled by regulated proteolysis of a transcription factor," *EMBO J*, vol. 17, no. 22, pp. 6730–8, 1998.

[20] W. K. Smits, C. C. Eschevins, K. A. Susanna, S. Bron, O. P. Kuipers, and L. W. Hamoen, "Stripping bacillus: Comk auto-stimulation is responsible for the bistable response in competence development," *Mol Microbiol*, vol. 56, no. 3, pp. 604–14, 2005.

[21] H. Maamar, A. Raj, and D. Dubnau, "Noise in gene expression determines cell fate in bacillus subtilis," *Science*, vol. 317, no. 5837, pp. 526–9, 2007.

[22] G. M. Süel, J. Garcia-Ojalvo, L. M. Liberman, and M. B. Elowitz, "An excitable gene regulatory circuit induces transient cellular differentiation," *Nature*, vol. 440, no. 7083, pp. 545–50, 2006.

[23] G. M. Süel, R. P. Kulkarni, J. Dworkin, J. Garcia-Ojalvo, and M. B. Elowitz, "Tunability and noise dependence in differentiation dynamics," *Science*, vol. 315, no. 5819, pp. 1716–9, 2007.

[24] T. Çağatay, M. Turcotte, M. B. Elowitz, J. Garcia-Ojalvo, and G. M. Süel, "Architecture-dependent noise discriminates functionally analogous differentiation circuits," *Cell*, vol. 139, no. 3, pp. 512–22, 2009.

[25] D. T. Gillespie, *Markov Processes: An Introduction for Physical Scientists*. Academic Press, 1991.

[26] D. T. Gillespie, "A general method for numerically simulating the stochastic time evolution of coupled chemical reactions," *Journal of Computational Physics*, vol. 22, no. 4, pp. 403–434, 1976.

[27] D. T. Gillespie, "Exact stochastic simulation of coupled chemical reactions," *J. Phys. Chem.*, vol. 81, no. 25, pp. 2340–2361, 1977.

[28] D. T. Gillespie, "Stochastic simulation of chemical kinetics," *Annu Rev Phys Chem*, vol. 58, pp. 35–55, 2007.

[29] Y. A. Kuznetsov, *Elements of applied bifurcation theory.* Applied mathematical sciences, New York u.a.: Springer, 3. ed., 2004.

[30] S. H. Strogatz, *Nonlinear dynamics and Chaos : with applications to physics, biology, chemistry, and engineering.* Studies in nonlinearity, Reading, Mass.: Addison-Wesley Pub., 1994.

[31] B. Ermentrout, *Simulating, analyzing, and animating dynamical systems : a guide to XPPAUT for researchers and students.* Software, environments, tools, Philadelphia: Society for Industrial and Applied Mathematics, 2002.

[32] E. D. Conrad, *Bifurcation Analysis and Qualitative Optimization of Models in Molecular Cell Biology with Applications to the Circadian Clock.* PhD thesis, Virginia Polytechnic Institute and State University, 2006.

[33] M. Turcotte, J. Garcia-Ojalvo, and G. M. Süel, "A genetic timer through noise-induced stabilization of an unstable state," *Proc Natl Acad Sci U S A*, vol. 105, no. 41, pp. 15732–7, 2008.

[34] N. G. van Kampen, *Stochastic processes in physics and chemistry.* North-Holland personal library, Amsterdam ; New York: North-Holland, 1992.

[35] M. Tabor, *Chaos and integrability in nonlinear dynamics : an introduction.* New York: Wiley, 1989.

[36] S. Kirkpatrick, J. Gelatt, C. D., and M. P. Vecchi, "Optimization by simulated annealing," *Science*, vol. 220, no. 4598, pp. 671–80, 1983.

[37] D. B. Fogel, "An introduction to simulated evolutionary optimization," *IEEE Trans Neural Netw*, vol. 5, no. 1, pp. 3–14, 1994.

[38] D. T. Gillespie, "Approximate accelerated stochastic simulation of chemically reacting systems," *Journal of Chemical Physics*, vol. 115, no. 4, pp. 1716–1733, 2001.

[39] S. Bhattacharya, Q. Zhang, and M. E. Andersen, "A deterministic map of waddington's epigenetic landscape for cell fate specification," *BMC Syst Biol*, vol. 5, p. 85, 2011.

[40] C. Li, E. Wang, and J. Wang, "Landscape and flux decomposition for exploring global natures of non-equilibrium dynamical systems under intrinsic statistical fluctuations," *Chemical Physics Letters*, vol. 505, no. 13, pp. 75–80, 2011.

BIOGRAPHICAL STATEMENT

The author Hongguang Xi was born in China. He received a Bachelor's Degree from China Agricultural University in the area of Applied Physics in 1996. He received a Master's degree from Tongji University in the area of Biomedical Engineering in 2007.

His research interests include numerical analysis, nonlinear dynamical systems, gene regulation and cell-fate decision, etc.. During the Master study and this thesis, he worked extensively on the study of complicated gene regulatory networks, algorithm implementation, and data analysis.

After graduating with his Master, he would like to go on pursuing a doctoral degree to further study the functionality of stochasticity in gene expression and to find key controlling factors in manipulating the dynamical features of the underlying gene circuits.